Dynamic magnetic phase transition induced by parametric magnon pumping

Jun-Yi Shan [1,2,*] Jonathan B. Curtis,[3,*] Mingyao Guo [1,2,*] Chang Jae Roh,[4,5] C. R. Rotundu [6] Young S. Lee,[6,7] Prineha Narang,[3] Tae Won Noh,[4,5] Eugene Demler,[8] and D. Hsieh [1,2,†]

[1]*Department of Physics, California Institute of Technology, Pasadena, California 91125, USA*
[2]*Institute for Quantum Information and Matter, California Institute of Technology, Pasadena, California 91125, USA*
[3]*College of Letters and Science, University of California, Los Angeles, California 90095, USA*
[4]*Center for Correlated Electron Systems, Institute for Basic Science (IBS), Seoul 08826, Republic of Korea*
[5]*Department of Physics and Astronomy, Seoul National University (SNU), Seoul 08826, Republic of Korea*
[6]*Stanford Institute for Materials and Energy Sciences, SLAC National Accelerator Laboratory, Menlo Park, California 94025, USA*
[7]*Department of Applied Physics, Stanford University, Stanford, California 94305, USA*
[8]*Institute for Theoretical Physics, ETH Zurich, 8093 Zurich, Switzerland*

Uncovering pathways to optically drive magnetic order-disorder transitions on ultrashort timescales can lead to the realization of novel out-of-equilibrium quantum phenomena. A long-sought pathway is to directly excite a highly nonthermal energy-momentum distribution of magnons, bypassing both charge and lattice degrees of freedom. However, this remains elusive owing to the weak coupling and large momentum mismatch between photons and magnons. Here we demonstrate strong parametric excitation of magnons across the entire Brillouin zone of the antiferromagnetic insulator $Sr_2Cu_3O_4Cl_2$ by periodically modulating the superexchange interaction with the electric field of light. The excitation efficiency is greatly enhanced by tuning to the van Hove singularity in the magnon spectrum, sufficient to transiently collapse the antiferromagnetic state using a pulsed laser field of 10^9 V/m. The order parameter recovery timescale increases by over 1000 times as a function of excitation density, reflecting a crossover from high- to low-energy magnon dominated decay dynamics. This electric-field induced parametric magnon pumping mechanism is applicable to a broad range of magnetic insulators and opens up the possibility of dynamically engineering magnon distributions by design.

I. INTRODUCTION

An extensively studied demagnetization pathway is through photothermal heating, whereby energy from a laser pulse is initially absorbed by the electronic or lattice subsystem and is subsequently transferred to the spin subsystem, raising the effective magnon temperature above the critical point [1–4]. This mechanism has been experimentally realized in many classes of materials ranging from ferromagnetic transition metals [5,6], rare earth metals [7], and doped III-V semiconductors [8] to antiferromagnetic transition metal oxide Mott insulators [9]. However, owing to the thermal origin of magnon excitations, the demagnetization timescale is limited by the rate of heat exchange between subsystems.

A distinct pathway to ultrafast demagnetization is through nonthermal excitation of magnons. However, this has been challenging to realize for two main reasons. First, the coupling between light and spin is inherently weak [10]. Second, the magnon density of states is typically largest for momenta near the Brillouin zone boundary, which far exceeds the momentum of light in the optical frequency range. In magnetic insulators, large momentum magnons can be indirectly excited via magnon-phonon [11] and magnon-exciton [12–15] absorption processes, photodoping [16–18], subwavelength confined optical fields [19] or extreme ultraviolet transient spin gratings [20]. However, while demagnetization can be reached in some of these cases, magnon generation is accompanied by electronic or lattice excitations. An alternative approach is to directly excite magnons using light that is far detuned from any electronic or phonon resonances. Although directly excited single magnons are confined near the zone center [21–25], finite momentum magnons can be directly excited via two-magnon processes. One established process is parametric pumping, where a counter-propagating magnon pair is selectively excited at half the frequency of a microwave magnetic field [26–28]. Another process is second-order impulsive stimulated Raman scattering, where magnon pairs are simultaneously excited throughout the Brillouin zone by an oscillating electric field far off-resonant from two-magnon energies [29–31]. So far, however, none of these processes have been shown to generate sufficiently high magnon densities to cause demagnetization for fluences up to tens of mJ/cm^2.

Here we demonstrate electric-field induced parametric pumping—a direct two-magnon excitation process allowed in locally noncentrosymmetric magnets—that enables both strong electric-dipole coupling and energy selectivity. Using the square-lattice cuprate antiferromagnetic Mott insulator $Sr_2Cu_3O_4Cl_2$ as a platform, we show that by selectively pumping a large nonthermal population of pure magnons around a van Hove singularity in the magnon spectrum located

*These authors contributed equally to this work.
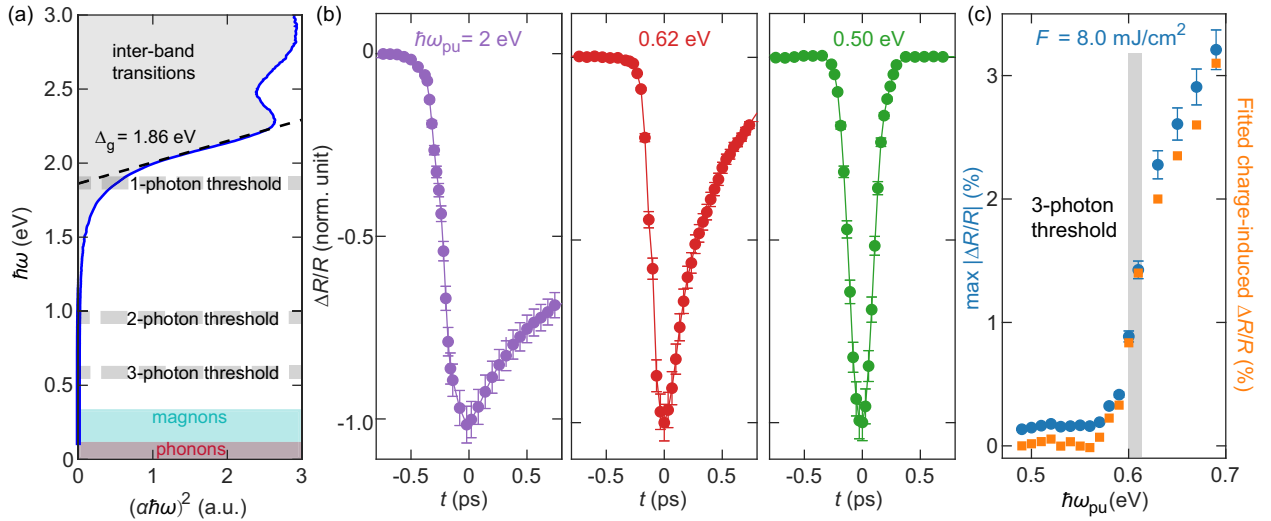†Corresponding author: dhsieh@caltech.edu

054302-1

FIG. 1. Suppressing multiphoton charge excitation in $Sr_2Cu_3O_4Cl_2$. (a) Tauc plot (blue curve) for $Sr_2Cu_3O_4Cl_2$ obtained from ellipsometry measurements taken at $T = 300$ K ($< T_{N,I} = 380$ K), where α is the absorption coefficient and $\hbar\omega$ is the photon energy. Dashed black line is a fit to a general model for interband absorption in a three-dimensional insulator [34,61], yielding $\Delta_g = 1.86$ eV. The energy range of phonons (magnons) is marked by a horizontal red (blue) bar. The threshold energies for one-, two-, and three-photon interband excitations are marked by dashed gray bars. (b) Normalized $\Delta R/R$ traces at $T = 300$ K for various $\hbar\omega_{pu}$, with $F = 1.4$, 8.0, and 8.0 mJ/cm^2 for the $\hbar\omega_{pu} = 2$, 0.62, and 0.50 eV traces, respectively. (c) Maximum ($t = 0$) value of $|\Delta R/R|$, superposed with the amplitude of the photocarrier contribution to $\Delta R/R$, plotted vs $\hbar\omega_{pu}$ for a fixed $F = 8.0$ mJ/cm^2. Assuming the 0.50 eV trace is purely coherent, we subtract it from traces taken at other pump photon energies to isolate the photocarrier contribution to $\Delta R/R$. These background subtracted traces are then fit to an exponential decay function over $0 < t < 700$ fs to extract an amplitude. The gray line denotes the three-photon threshold. All error bars represent the standard error of the mean from fifteen independent measurements.

near the zone boundary, ultrafast demagnetization can be realized with pulsed fields of 1.1×10^9 V/m (corresponding to a fluence $F = 19.2$ mJ/cm^2).

II. MINIMIZING MULTIPHOTON CHARGE EXCITATION

The hierarchy of energy scales in copper-oxide based square lattice spin-1/2 Mott antiferromagnets is particularly suitable for demonstrating this phenomenon. Strong nearest-neighbor magnetic exchange interactions give rise to large magnon energies ($\hbar\omega_{mag}$) in the mid-infrared range, which is conducive to strong-field driving. Moreover, in certain compounds, the magnon bandwidth exceeds the phonon bandwidth by several times while the charge gap (Δ_g) exceeds twice the magnon bandwidth by several times. For $Sr_2Cu_3O_4Cl_2$, inelastic neutron scattering and Raman spectroscopy [32,33] experiments report maximum magnon and phonon energies of approximately 0.3 and 0.08 eV, respectively. Our ellipsometry measurements show $\Delta_g = 1.86$ eV [Fig. 1(a)] [34]. This provides a large energy window for parametric magnon pumping that is far detuned from resonant electronic and lattice excitations.

Nevertheless, in the high field regime, charge excitations can still be made with pump photon energies ($\hbar\omega_{pu}$) below Δ_g via nonlinear processes such as multiphoton absorption and Zener tunneling [35,36]. To verify the existence of an energy window across $2\hbar\omega_{mag}$ that is sufficiently transparent to nonlinear charge excitation, we performed time-resolved optical reflectivity measurements as a function of $\hbar\omega_{pu}$ on $Sr_2Cu_3O_4Cl_2$ single crystals. The probe photon energy was tuned near Δ_g to enhance sensitivity to photocarrier popula-

tion. For above-gap pumping ($\hbar\omega_{pu} = 2$ eV), the differential reflectivity transient ($\Delta R/R$) is clearly asymmetric about time $t = 0$—the instant of pump probe overlap—characteristic of rapid photocarrier generation followed by slower relaxation [Fig. 1(b)]. Upon lowering $\hbar\omega_{pu}$ below Δ_g, the reflectivity transient gradually evolves to being perfectly symmetric about $t = 0$, mimicking the pump probe cross correlation. This signifies a purely coherent response due to pump field dressing of the electronic bands [37], with no measurable photocarrier production. For a fixed pump fluence of $F = 8.0$ mJ/cm^2, we find that the crossover to a predominantly coherent lineshape occurs below $\hbar\omega_{pu} \sim 0.6$ eV, which is the threshold for three-photon absorption ($\Delta_g/3$). This crossover can also be clearly visualized by plotting the magnitude of $\Delta R/R$ at $t = 0$ (or the amplitude of the photocarrier contribution to $\Delta R/R$) versus $\hbar\omega_{pu}$ [Fig. 1(c)], which exhibits a drop as the photocarrier contribution to $\Delta R/R$ is suppressed below $\Delta_g/3$. These results are consistent with the Keldysh parameter $\hbar\omega_{pu}/(eE_{pu}\xi) > 2$ calculated using relevant experimental values (e is the electron charge, ξ is the electron-hole correlation length, and E_{pu} is the peak pump field strength), which locates the system in the multiphoton dominated regime.

III. ENERGY-SELECTIVE MAGNON PUMPING INDUCED DEMAGNETIZATION

The structure of $Sr_2Cu_3O_4Cl_2$ consists of a stack of square-net layers similar to the parent compounds of high-temperature superconducting cuprates. However, at the center of every other plaquette of the conventional CuO_2
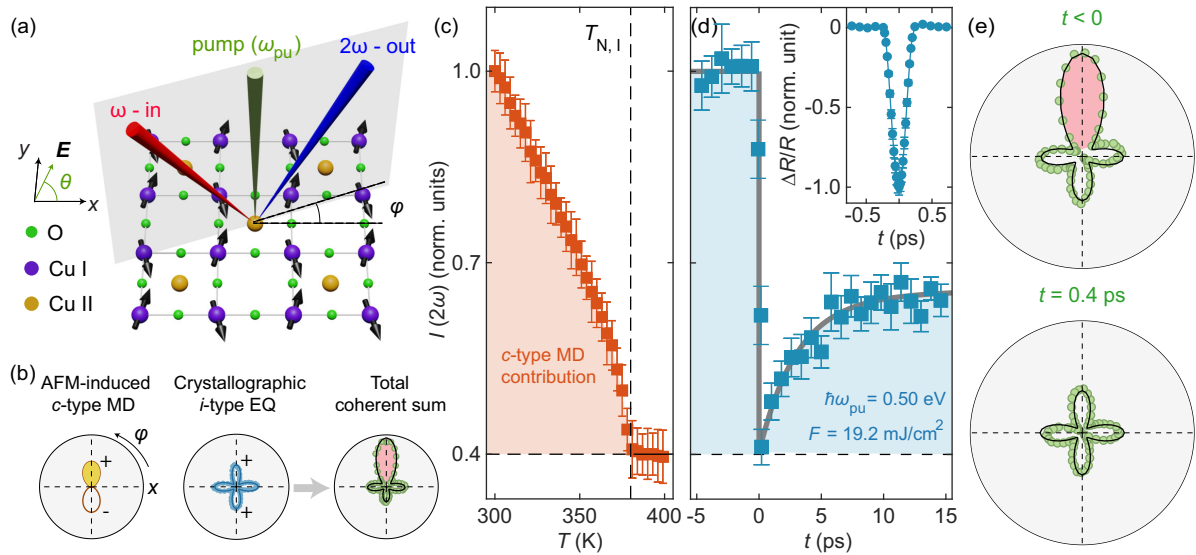
FIG. 2. Nonthermal magnon-induced magnetic order collapse. (a) Ordered Cu_I spin arrangement (arrows) below $T_{N,I}$. Canting angles are exaggerated for clarity. The probe beam (red) is focused obliquely onto the Cu_3O_4 plane, and the reflected SHG intensity (blue) is measured as a function of the scattering plane angle φ. Both incident and reflected beams are linearly polarized in the scattering plane (gray shade). The pump beam (green) is incident with linear polarization along θ. (b) The c-type MD and i-type EQ contributions to the RA SHG signal and their coherent sum. Markers in the middle and right panels are the measured RA SHG patterns above (400 K) and below (300 K) $T_{N,I}$, respectively. Solid lines are symmetry-based fits [34]. Different shades in the left panel represent opposite phases. (c) Temperature-dependent static SHG intensity acquired at $\varphi = 90°$ [(pink lobe in (b)] normalized to its value at 300 K. The nonmagnetic (i-type EQ) background value is denoted by a horizontal dashed line. (d) Time-resolved SHG intensity at $\varphi = 90°$ for $\hbar\omega_{pu} = 0.5$ eV and $F = 19.2$ mJ/cm^2, plotted on the same scale as (c). Measurements were taken at $T = 300$ K. Gray line is a guide to the eye. Inset shows $\Delta R/R$ taken with the same pump parameters. All error bars represent the standard error of the mean from four independent measurements. (e) RA SHG data (green circles) measured at $t < 0$ and $t = 0.4$ ps, overlaid with fits to (MD + EQ) and solely EQ contributions, respectively (black curves). We chose $t = 0.4$ ps to represent the instant of maximum demagnetization to avoid coherent artifacts near $t = 0$ [37].

square net (the Cu_I sublattice), there exists an additional Cu ion (the Cu_{II} sublattice), which removes the center of inversion located between neighboring Cu_I sites but preserves global inversion symmetry [Fig. 2(a)]. The nearest-neighbor Cu_I-Cu_I antiferromagnetic (AFM) exchange coupling ($J_1 = 130$ meV) exceeds that for Cu_I-Cu_{II} and Cu_{II}-Cu_{II} by over an order of magnitude. Therefore the Cu_I sublattice orders at a much higher temperature ($T_{N,I} \approx 380$ K) compared to the Cu_{II} sublattice ($T_{N,II} \approx 40$ K) [38]. However, the interaction between the AFM ordered Cu_I sublattice and the paramagnetic Cu_{II} sublattice below $T_{N,I}$ induces a weak in-plane magnetization **M** along one out of four possible Cu_I-Cu_I bond directions [39], breaking the fourfold (C_4) rotational symmetry of the underlying square lattice [Fig. 2(a)].

A previous study [40] showed that the loss of rotational symmetry below $T_{N,I}$ activates a bulk magnetic-dipole (MD) optical second harmonic generation (SHG) process of the form $P_i(2\omega) = \chi_{ijk}^{MD} E_j(\omega) H_k(\omega)$. Here χ_{ijk}^{MD} is a time-reversal odd (c-type) susceptibility tensor that couples linearly to **M**, $E_j(\omega)$ and $H_k(\omega)$ are the electric and magnetic fields of the incident probe light at frequency ω, $P_i(2\omega)$ is the polarization induced at the second harmonic, and the indices run through x, y, and z. Interference between this MD contribution and a temperature-independent time-reversal even (i-type) bulk electric-quadrupole (EQ) contribution produces a rotational anisotropy (RA) SHG pattern with C_1 symmetry [Fig. 2(b)], whose orientation is locked to **M**. This provides a unique opportunity to measure the demagnetization dy-

namics of a cuprate Mott AFM (Cu_I) using time-resolved RA SHG.

We carried out time-resolved RA SHG measurements using a high-speed rotating scattering plane technique [41]. The fundamental probe photon energy was fixed at 1.55 eV while the pump photon energy was varied across the window over which multiphoton absorption is suppressed. Both pump and probe beams were focused within a single magnetic domain [34,40]. Figure 2(c) shows the temperature-dependent intensity of the largest lobe in the RA SHG pattern—corresponding to the scattering plane angle $\varphi = 90°$ [Fig. 2(a)]—in the absence of pumping. The emergence of a temperature-dependent MD contribution atop a temperature-independent EQ background is clearly observed below $T_{N,I}$. The pump beam is then introduced with the sample held at $T = 300$ K. Figure 2(d) shows the instantaneous SHG intensity at $\varphi = 90°$ as a function of time delay relative to a pump pulse with $\hbar\omega_{pu} = 0.50$ eV and $F = 19.2$ mJ/cm^2, plotted on the same intensity scale as Fig. 2(c). At $t = 0$ there is an abrupt intensity drop from the equilibrium $T = 300$ K value down to the EQ background value, signifying a complete suppression of the MD contribution. Full collapse of the AFM state is further corroborated by instantaneous RA patterns acquired around $t = 0$, which show that only a C_4 symmetric EQ contribution remains [Fig. 2(e)]. The absence of any measurable photocarrier population [Fig. 2(d), inset] suggests that the demagnetization is driven entirely by nonthermal magnons [34]. We also note that the resolution limited (<100 fs) demagnetization dy-
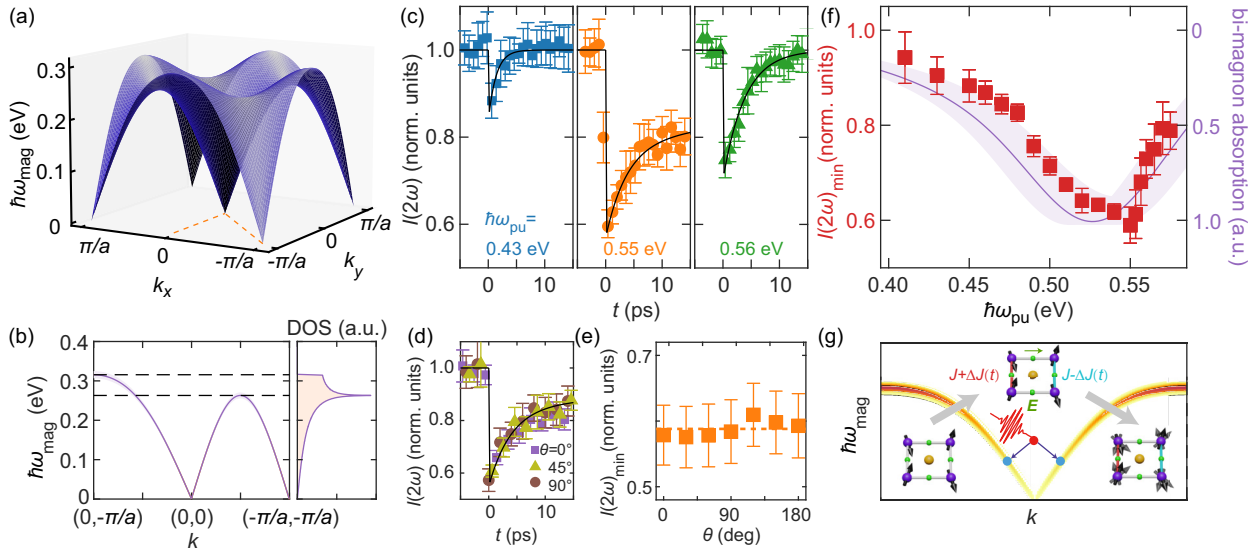
FIG. 3. Parametric magnon pair generation. (a) In-plane ($k_z = 0$) magnon dispersion of the Cu_I sublattice of $Sr_2Cu_3O_4Cl_2$ calculated using the SPINW code [62] and a J_1-J_2 model. Values of the nearest- and next nearest-neighbor exchange ($J_1 = 130$ meV, $J_2 = -32.5$ meV) are determined from experiments [32,42,43]. The k_x and k_y axes coincide with the x and y directions in Fig. 2(a). (b) Magnon dispersion along high-symmetry cuts [dashed line in (a)]. The shaded region in the left panel represents the uncertainty in the magnon energy, originating from slight differences in the exchange energies reported in the literature [32,42,43]. Horizontal dashed lines indicate van Hove singularities in the magnon density of states (DOS). (c) Transient SHG intensity for select $\hbar\omega_{pu}$ and fixed $F = 8.0$ mJ/cm². Black lines are guides to the eye. (d) Transient SHG intensity for select pump polarization angles (θ) for fixed $\hbar\omega_{pu} = 0.55$ eV and $F = 8.0$ mJ/cm². Black line is a guide to the eye. (e) Value of the SHG transient at $t = 0.4$ ps as a function of θ with the same pump conditions as (d). (f) Value of the SHG transient at $t = 0.4$ ps (red markers) as a function of $\hbar\omega_{pu}$ for fixed $F = 8.0$ mJ/cm². Purple curve shows the calculated bimagnon absorption coefficient convolved with a 0.04 eV instrument spectral width. Shaded region represents the range over which the bimagnon absorption coefficient varies using the range of different magnon energies plotted in (b). All measurements were taken at $T = 300$ K. All error bars represent the standard error of the mean from four independent measurements. (g) Schematic of the parametric generation process where a photon with energy $\hbar\omega_{pu}$ converts into a magnon pair with equal energy $\hbar\omega_{mag} = \hbar\omega_{pu}/2$ and opposite momentum. (Inset) Microscopically, light polarized along the x direction (green arrow) temporally modulates the superexchange along the vertical bonds, with opposite bonds modulated by opposite signs owing to inversion symmetry.

namics is consistent with the fast timescale associated with Cu_I-Cu_I exchange ($h/J_1 \approx 30$ fs, where h is Planck's constant), but is incompatible with the slow timescale associated with Cu_I-Cu_{II} pseudodipolar coupling (≈ 200 ps) that is responsible for the finite **M** [39]. This rules out the possibility that the pump pulse is merely suppressing **M** by reducing the Cu_I-Cu_{II} coupling, in turn decreasing the canting angle of the magnetic moments, while leaving long-range AFM order of Cu_I intact.

To ascertain whether the nonthermal magnons are excited in pairs with energy selectivity, we performed pump photon energy dependent measurements. Figure 3(a) shows a linear spin-wave calculation for $Sr_2Cu_3O_4Cl_2$ based on a two-dimensional Heisenberg model that includes nearest- and next-nearest-neighbor Cu_I-Cu_I exchange energies fitted to experiments on $Sr_2Cu_3O_4Cl_2$ and its closely related compounds $Sr_2CuO_2Cl_2$ and $Ba_2Cu_3O_4Cl_2$ [32,34,42,43]. There are van Hove singularities at two distinct momenta in the Brillouin zone: a saddle point at $(-\pi/2a, -\pi/2a)$ and a maximum at $(0, -\pi/a)$—where a is the Cu_I-Cu_I bond length—that gives rise to a magnon density of states (DOS) that diverges at $\hbar\omega_{mag} \approx 0.26$ eV and vanishes sharply above around 0.31 eV [Fig. 3(b)] [44]. The two-magnon absorption rate (Γ) depends on the magnon DOS at $\hbar\omega_{pu}/2$ according to Fermi's golden

rule:

$$\Gamma = \sum_{\mathbf{k}} \frac{2\pi}{\hbar^2} |\langle 2M(\mathbf{k})|H_c|g\rangle|^2 \delta(2\hbar\omega_{mag}(\mathbf{k}) - \hbar\omega_{pu}), \quad (1)$$

where the sum is over the Brillouin zone, $|g\rangle$ is the magnetic ground state, $|2M(\mathbf{k})\rangle$ is the state with a pair of magnons excited at momenta $\pm\mathbf{k}$, H_c is the light-spin coupling Hamiltonian, and $\delta(\cdot)$ is the Dirac delta function. Therefore a signature of energy-selective magnon pair generation in $Sr_2Cu_3O_4Cl_2$ is a demagnetization efficiency that reaches a maximum when $\hbar\omega_{pu}/2$ coincides with the DOS peak. We measured SHG transients analogous to Fig. 2(d) over a range of $\hbar\omega_{pu}$ within the window where multiphoton absorption is suppressed, keeping both the pump pulse duration and F (8.0 mJ/cm²) constant. The level of demagnetization near $t = 0$ is a clearly nonmonotonic function of $\hbar\omega_{pu}$ [Fig. 3(c)] and exhibits a maximum near 0.55 eV [Fig. 3(f)] [34], consistent with twice the DOS peak. To make sense of the measured line shape, it is necessary to first understand the light-spin coupling mechanism that controls the matrix element in Eq. (1).

IV. THE ELECTRIC-FIELD INDUCED PARAMETRIC MAGNON PUMPING MECHANISM

Photoexcitation of magnon pairs in AFM insulators has been extensively studied in the context of Raman and infrared absorption spectroscopy. Three main mechanisms have been put forward [45]: (a) electric-dipole coupling mediated by spin-orbit interactions, (b) direct magnetic-dipole coupling, and (c) electric-dipole coupling realized through photoassisted spin exchange [46]. Mechanism (a) is unlikely to be dominant in $Sr_2Cu_3O_4Cl_2$ owing to the weak spin-orbit coupling in cuprates. Mechanism (b) can also be ruled out because the magnetic-dipole Hamiltonian involves a dot product between the magnetic moment and the magnetic field of the pump light [34]. Yet there is no measurable change in the demagnetization efficiency as the angle (θ) of a linearly polarized pump beam [Fig. 2(a)] is varied with respect to the direction of ordered moments [Figs. 3(d) and 3(e)].

Mechanism (c) originates from a spin-dependent electric polarization for two-magnon excitations of the form

$$\mathbf{P} = \sum_{\langle ij \rangle} \mathbf{\Pi}_{ij} \mathbf{S}_i \cdot \mathbf{S}_j, \tag{2}$$

where the sum is over spins $\mathbf{S}$ on neighboring sites i and j and $\mathbf{\Pi}_{ij}$ is a phenomenological vector coupling strength. By symmetry, $\mathbf{\Pi}_{ij}$ transforms like a vector and is therefore nonvanishing if the mid-point of the $\langle ij \rangle$ bond is not a crystallographic inversion center [46], which is the case for $Sr_2Cu_3O_4Cl_2$. We note that an overall inversion symmetry of the lattice does not dictate whether $\mathbf{P}$ is vanishing or not [34]. This enables an electric-dipole coupling of light to $\pm \boldsymbol{k}$ magnon pairs of the form $H_c = -\mathbf{P} \cdot \mathbf{E}_{pu} \cos \omega_{pu} t$, even in the absence of spin-orbit coupling or global inversion symmetry breaking. Physically, this represents a parametric magnon pumping process. As the equilibrium Heisenberg Hamiltonian with superexchange J_1 is dressed by H_c, the effective exchange along the $\langle ij \rangle$ bond becomes $J_1 + \Delta J_{ij}(t) = J_1 - \mathbf{E}_{pu} \cdot \mathbf{\Pi}_{ij} \cos \omega_{pu} t$, imparting a time-periodic modulation of J_1 at the pump frequency. In the case where the pump photon is absorbed (as opposed to inelastically scattered), the two magnons are created exclusively at $\hbar \omega_{mag}(\pm \boldsymbol{k}) = \hbar \omega_{pu}/2$ by conservation of energy and momentum [Fig. 3(g)] [34]. We note that there could also be an additional contribution to $\mathbf{P}$ that is proportional to the pump field $\mathbf{E}_{pu}$ [47]. However, this would result in a Hamiltonian term that is quadratic in $\mathbf{E}_{pu}$, corresponding to an inelastic Raman scattering process [48,49] where the magnon pairs are excited at energies much smaller than $\hbar \omega_{pu}$, which is inconsistent with our resonant photon absorption process.

By rewriting Eqn. (2) in terms of magnon operators and taking into account the C_4 symmetry of the $Sr_2Cu_3O_4Cl_2$ lattice, the matrix element $|\langle 2M(\boldsymbol{k})|H_c|g \rangle|^2$ can be shown to be proportional to $\sin^2 k_x a + \sin^2 k_y a$ [34]. Using this expression we find that the bi-magnon absorption coefficient, which scales like $\Gamma \times \hbar \omega_{pu}$, is independent of θ, in agreement with experiment [Fig. 3(e)]. Moreover, the calculated $\hbar \omega_{pu}$ dependence [34], convolved with our experimental energy resolution function, agrees well with the measured demagnetization efficiency curve [Fig. 3(f)]. Collectively these data

support energy-selective parametric magnon pumping as the origin of the observed demagnetization.

V. RELAXATION OF THE NONTHERMAL MAGNON BATH

Our parametric magnon pumping mechanism provides an opportunity to study out-of-equilibrium magnon dynamics starting from a well-defined nonthermal distribution, without the presence of other optically excited quasiparticles. Figure 4(a) shows SHG transients measured with $\hbar \omega_{pu} = 0.55$ eV in a weak magnon pumping regime where the order parameter reduction at $t = 0$ is relatively small [Fig. 4(a), inset]. Here we observe complete recovery back to the $t < 0$ value on a fast timescale (τ_1) of several picoseconds. In contrast, upon entering a stronger magnon pumping regime where the demagnetization is more significant, a slow recovery component (τ_2) on the hundreds of picoseconds timescale emerges atop the τ_1 component, becoming increasingly dominant as the pump fluence approaches and crosses the threshold for full demagnetization [Fig. 4(b)].

These observations can be comprehensively explained as follows. High-energy magnon pairs at $\pm(k_x, k_y, k_z)$ are initially excited in the three-dimensional Brillouin zone along an isoenergetic surface at $\hbar \omega_{pu}/2$, which is highly anisotropic owing to the weak inter-layer exchange ($J_c \approx 10^{-4} J_1$) in $Sr_2Cu_3O_4Cl_2$ [Fig. 4(c)]. These high-energy magnons then disappear primarily via three processes: (i) emission into the surrounding un-pumped regions; (ii) annihilation by scattering with optical phonons; or (iii) internal thermalization through anharmonic magnon-magnon interactions, leading to the decay of high-energy magnons to a quasi-thermal anisotropic distribution of low-energy magnons [Fig. 4(c)]. Since all three processes generally occur on the timescale of a picosecond [16,50,51], we attribute the τ_1 component to the loss of high-energy magnons. In contrast, owing to a drastically reduced phase space for low-energy magnon-phonon scattering, the low-energy magnons cool very slowly—on the timescale of a nanosecond in comparable layered AFM insulators [16]. Thus, we attribute the τ_2 component to cooling of the low-energy magnon distribution.

Theoretical models [52] suggest that the efficiency of process (iii) in the previous paragraph increases with the initial density of high-energy magnons. Therefore the weak pumping regime is dominated by processes (i) and (ii). Here, the density of resulting low-energy magnons is too low to impart any measurable change in the order parameter, so no τ_2 component is detected. The observed increase in τ_1 with increasing pump fluence [Fig. 4(d)] possibly originates from a density dependent downward renormalization of J_1 [53–55], as higher magnon densities lead to lower precession frequencies thus slower dissipation, assuming a constant energy dissipated per precession period [50]. In the strong pumping regime, the τ_2 component becomes measurable owing to the higher efficiency of process (iii), with both its amplitude and timescale continuing to increase with pump fluence. Above the fluence ($F_c = 14$ mJ/cm^2) where the initial density of high-energy magnons reaches the threshold for full demagnetization at $t = 0$, a small τ_1 component can still be resolved atop a large
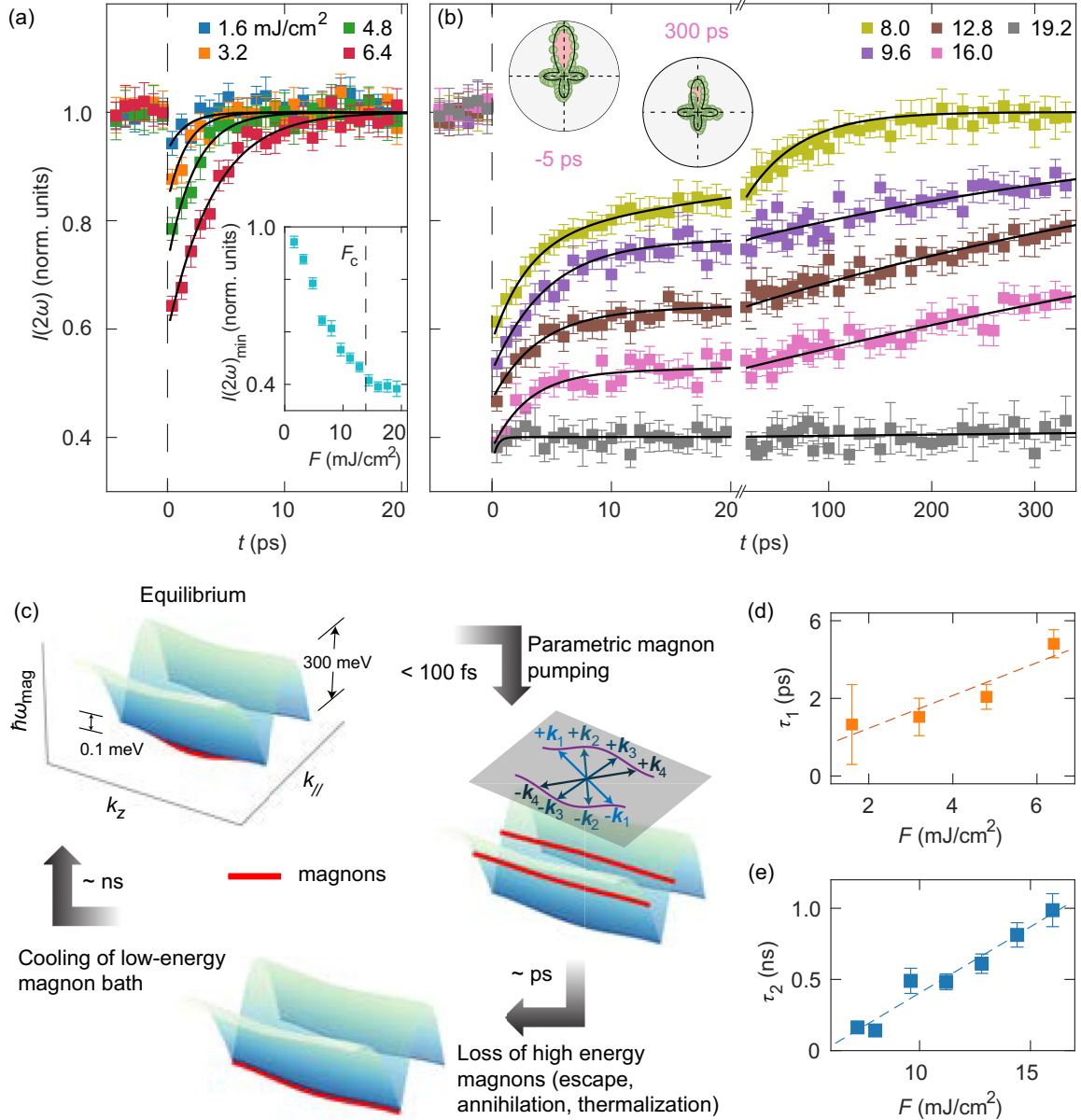
FIG. 4. Out-of-equilibrium relaxation dynamics of the magnon bath. Time-resolved SHG transients measured at $T = 300$ K, $\varphi = 90°$, and $\hbar\omega_{pu} = 0.55$ eV for select pump fluences in the (a) weak and (b) strong pumping regimes. Fits to a biexponential function of the form $\chi_{ijk}^{MD}(t) = \chi_{ijk}^{MD}(t < 0) - A_1 \exp(-t/\tau_1) - A_2 \exp(-t/\tau_2)$ are overlaid (black lines). Inset in a shows the fluence dependence of the minimum SHG intensity and the inset in b shows RA SHG patterns at select time delays for $F = 16$ mJ/cm^2. Error bars represent the standard error of the mean from fifteen independent measurements. Since $\hbar\omega_{pu} = 0.55$ eV is close to $\Delta_g/3$, we also acquired $\Delta R/R$ traces at this photon energy to check for multiphoton absorption. Slight asymmetry about $t = 0$ was only measurable for fluences above around 12.8 mJ/cm^2 [34]. (c) Schematic of the multistage relaxation process. The magnon dispersion is plotted vs in-plane ($k_\parallel$) and out-of-plane (k_z) momentum. The dispersion along k_z is exaggerated for clarity. The magnon occupation at each stage (red) is overlaid. The gray shaded plane shows different possible momentum combinations of excited magnon pairs. (d) Fitted values of τ_1 and (e) τ_2 as a function of fluence. Error bars represent the fitting uncertainties.

τ_2 component [see the $F = 16.0$ mJ/cm^2 curve in Fig. 4(b)]. Upon reaching an even higher fluence ($F^* = 19$ mJ/cm^2), the τ_1 component becomes negligible, indicating a second threshold where the density of low-energy magnons alone is sufficiently high to induce full demagnetization. The value of τ_2 becomes very large at F^*—far exceeding our measurement time window—potentially signaling a divergence due to

critical slowing down at a quasithermal phase transition [34,51] [Fig. 4(e)]. We note that the magnon density continues to increase with fluence even above F_c because the transiently demagnetized state can still support short-range intralayer AFM correlations and intralayer paramagnons despite the absence of interlayer coherence due to the pronounced exchange anisotropy of Sr$_2$Cu$_3$O$_4$Cl$_2$.

VI. CONCLUSION AND OUTLOOK

The electric-field induced parametric magnon pumping phenomenon demonstrated here is expected to be active across a wide range of AFM insulators with broken local inversion symmetry. While local inversion is broken by the additional Cu_{II} sublattice in $Sr_2Cu_3O_4Cl_2$, it can also be broken by metal-ligand-metal bond buckling, which is a common feature of cuprates and transition metal oxides more generally. Provided the energy of van Hove singularities in the magnon spectrum is sufficiently detuned from electronic and phonon resonances, our protocol can be used to rapidly turn off magnetic order in these systems by directly engineering the magnon bath. Through temporal and spectral shaping of the pump pulse, highly tailored nonthermal magnon distributions can be created, opening up new possibilities for realizing exotic collective phenomena beyond demagnetization [56], such as magnon Bose-Einstein condensation [26], topological magnonic states [57], and superconductivity mediated by drive-enhanced spin fluctuations [58,59].

Note added. Recently, we became aware of another work [60] discussing resonant electric-field induced pumping of zone-edge magnons in hematite. However, this work was focused on modifying the magnon spectrum and did not report demagnetization.

[1] A. Kirilyuk, A. V. Kimel, and T. Rasing, Ultrafast optical manipulation of magnetic order, Rev. Mod. Phys. **82**, 2731 (2010).

[2] B. Koopmans, G. Malinowski, F. Dalla Longa, D. Steiauf, M. Fähnle, T. Roth, M. Cinchetti, and M. Aeschlimann, Explaining the paradoxical diversity of ultrafast laser-induced demagnetization, Nat. Mater. **9**, 259 (2010).

[3] S. L. Johnson, M. Savoini, P. Beaud, G. Ingold, U. Staub, F. Carbone, L. Castiglioni, M. Hengsberger, and J. Osterwalder, Watching ultrafast responses of structure and magnetism in condensed matter with momentum-resolved probes, Struct. Dyn. **4**, 061506 (2017).

[4] A. V. Kimel, R. V. Pisarev, J. Hohlfeld, and T. Rasing, Ultrafast quenching of the antiferromagnetic order in $FeBO_3$: Direct optical probing of the phonon-magnon coupling, Phys. Rev. Lett. **89**, 287401 (2002).

[5] E. Beaurepaire, J.-C. Merle, A. Daunois, and J.-Y. Bigot, Ultrafast spin dynamics in ferromagnetic nickel, Phys. Rev. Lett. **76**, 4250 (1996).

[6] P. Tengdin, W. You, C. Chen, X. Shi, D. Zusin, Y. Zhang, C. Gentry, A. Blonsky, M. Keller, P. M. Oppeneer *et al.*, Critical behavior within 20 fs drives the out-of-equilibrium laser-induced magnetic phase transition in nickel, Sci. Adv. **4**, eaap9744 (2018).

[7] A. Vaterlaus, T. Beutler, and F. Meier, Spin-lattice relaxation time of ferromagnetic gadolinium determined with time-resolved spin-polarized photoemission, Phys. Rev. Lett. **67**, 3314 (1991).

[8] E. Kojima, R. Shimano, Y. Hashimoto, S. Katsumoto, Y. Iye, and M. Kuwata-Gonokami, Observation of the spin-charge thermal isolation of ferromagnetic $Ga_{0.94}Mn_{0.06}$ As by time-resolved magneto-optical measurements, Phys. Rev. B **68**, 193203 (2003).

[9] J. A. Johnson, T. Kubacka, M. C. Hoffmann, C. Vicario, S. de Jong, P. Beaud, S. Grübel, S.-W. Huang, L. Huber, Y. W. Windsor, E. M. Bothschafter, L. Rettig, M. Ramakrishnan, A. Alberca, L. Patthey, Y.-D. Chuang, J. J. Turner, G. L. Dakovski, W.-S. Lee, M. P. Minitti *et al.*, Magnetic order dynamics in optically excited multiferroic $TbMnO_3$, Phys. Rev. B **92**, 184429 (2015).

[10] A. G. Gurevich and G. A. Melkov, *Magnetization Oscillations and Waves* (CRC Press, London, 2020).

[11] J. Lorenzana and G. A. Sawatzky, Phonon assisted multimagnon optical absorption and long lived two-magnon states in undoped lamellar copper oxides, Phys. Rev. Lett. **74**, 1867 (1995).

[12] D. D. Sell, R. L. Greene, and R. M. White, Optical exciton-magnon absorption in MnF_2, Phys. Rev. **158**, 489 (1967).

[13] J. S. Dodge, A. B. Schumacher, J.-Y. Bigot, D. S. Chemla, N. Ingle, and M. R. Beasley, Time-resolved optical observation of spin-wave dynamics, Phys. Rev. Lett. **83**, 4650 (1999).

[14] D. Bossini, K. Konishi, S. Toyoda, T.-H. Arima, J. Yumoto, and M. Kuwata-Gonokami, Femtosecond activation of magnetoelectricity, Nat. Phys. **14**, 370 (2018).

[15] K. Tsutsui, K. Shinjo, S. Sota, and T. Tohyama, Exciton-assisted low-energy magnetic excitations in a photoexcited Mott insulator on a square lattice, Commun. Phys. **6**, 41 (2023).

[16] M. P. M. Dean, Y. Cao, X. Liu, S. Wall, D. Zhu, R. Mankowsky, V. Thampy, X. M. Chen, J. G. Vale, D. Casa, J. Kim, A. H. Said, P. Juhas, R. Alonso-Mori, J. M. Glownia, A. Robert, J.

Robinson, M. Sikorski, S. Song, M. Kozina *et al.*, Ultrafast energy- and momentum-resolved dynamics of magnetic correlations in the photo-doped Mott insulator Sr_2IrO_4, Nat. Mater. **15**, 601 (2016).

[17] J.-A. Yang, N. Pellatz, T. Wolf, R. Nandkishore, and D. Reznik, Ultrafast magnetic dynamics in insulating $YBa_2Cu_3O_{6.1}$ revealed by time resolved two-magnon Raman scattering, Nat. Commun. **11**, 2548 (2020).

[18] D. G. Mazzone, D. Meyers, Y. Cao, J. G. Vale, C. D. Dashwood, Y. Shi, A. J. A. James, N. J. Robinson, J. Lin, V. Thampy, Y. Tanaka, A. S. Johnson, H. Miao, R. Wang, T. A. Assefa, J. Kim, D. Casa, R. Mankowsky, D. Zhu, R. Alonso-Mori *et al.*, Laser-induced transient magnons in $Sr_3Ir_2O_7$ throughout the Brillouin zone, Proc. Natl. Acad. Sci. USA **118**, e2103696118 (2021).

[19] J. R. Hortensius, D. Afanasiev, M. Matthiesen, R. Leenders, R. Citro, A. V. Kimel, R. V. Mikhaylovskiy, B. A. Ivanov, and A. D. Caviglia, Coherent spin-wave transport in an antiferromagnet, Nat. Phys. **17**, 1001 (2021).

[20] D. Ksenzov, A. A. Maznev, V. Unikandanunni, F. Bencivenga, F. Capotondi, A. Caretta, L. Foglia, M. Malvestuto, C. Masciovecchio, R. Mincigrucci, K. A. Nelson, M. Pancaldi, E. Pedersoli, L. Randolph, H. Rahmann, S. Urazhdin, S. Bonetti, and C. Gutt, Nanoscale transient magnetization gratings created and probed by femtosecond extreme ultraviolet pulses, Nano Lett. **21**, 2905 (2021).

[21] A. V. Kimel, A. Kirilyuk, P. A. Usachev, R. V. Pisarev, A. M. Balbashov, and T. Rasing, Ultrafast non-thermal control of magnetization by instantaneous photomagnetic pulses, Nature (London) **435**, 655 (2005).

[22] T. Kampfrath, A. Sell, G. Klatt, A. Pashkin, S. Mährlein, T. Dekorsy, M. Wolf, M. Fiebig, A. Leitenstorfer, and R. Huber, Coherent terahertz control of antiferromagnetic spin waves, Nat. Photonics **5**, 31 (2011).

[23] E. A. Mashkovich, K. A. Grishunin, R. M. Dubrovin, A. K. Zvezdin, R. V. Pisarev, and A. V. Kimel, Terahertz light-driven coupling of antiferromagnetic spins to lattice, Science **374**, 1608 (2021).

[24] K. Yamaguchi, M. Nakajima, and T. Suemoto, Coherent control of spin precession motion with impulsive magnetic fields of half-cycle terahertz radiation, Phys. Rev. Lett. **105**, 237201 (2010).

[25] D. M. Juraschek, D. S. Wang, and P. Narang, Sum-frequency excitation of coherent magnons, Phys. Rev. B **103**, 094407 (2021).

[26] S. O. Demokritov, V. E. Demidov, O. Dzyapko, G. A. Melkov, A. A. Serga, B. Hillebrands, and A. N. Slavin, Bose-Einstein condensation of quasi-equilibrium magnons at room temperature under pumping, Nature (London) **443**, 430 (2006).

[27] J. Bailey, P. Sukhachov, K. Baumgaertl, S. Finizio, S. Wintz, C. Dubs, J. Raabe, D. Grundler, A. Balatsky, and G. Aeppli, Multi-band Bose-Einstein condensate at four-particle scattering resonance, arXiv:2201.11043.

[28] T. X. Zhou, J. J. Carmiggelt, L. M. Gächter, I. Esterlis, D. Sels, R. J. Stöhr, C. Du, D. Fernandez, J. F. Rodriguez-Nieva, F. Büttner, E. Demler, and A. Yacoby, A magnon scattering platform, Proc. Natl. Acad. Sci. USA **118**, e2019473118 (2021).

[29] J. Zhao, A. V. Bragas, D. J. Lockwood, and R. Merlin, Magnon squeezing in an antiferromagnet: Reducing the spin noise below the standard quantum limit, Phys. Rev. Lett. **93**, 107203 (2004).

[30] D. Bossini, S. Dal Conte, Y. Hashimoto, A. Secchi, R. V. Pisarev, T. Rasing, G. Cerullo, and A. V. Kimel, Macrospin dynamics in antiferromagnets triggered by sub-20 femtosecond injection of nanomagnons, Nat. Commun. **7**, 10645 (2016).

[31] D. Bossini, A. M. Kalashnikova, R. V. Pisarev, T. Rasing, and A. V. Kimel, Controlling coherent and incoherent spin dynamics by steering the photoinduced energy flow, Phys. Rev. B **89**, 060405(R) (2014).

[32] J. Holmlund, C. S. Knee, J. Andreasson, M. Granath, A. P. Litvinchuk, and L. Börjesson, Two-magnon Raman scattering from the Cu_3O_4 layers in $(Sr_2, Ba_2)Cu_3O_4Cl_2$, Phys. Rev. B **79**, 085109 (2009).

[33] A. Zibold, H. L. Liu, S. W. Moore, J. M. Graybeal, and D. B. Tanner, Optical properties of single-crystal $Sr_2CuO_2Cl_2$, Phys. Rev. B **53**, 11734 (1996).

[34] See Supplemental Material at http://link.aps.org/supplemental/10.1103/PhysRevB.109.054302 for further details of the experimental methods and supporting data which includes Refs. [63–71].

[35] X. Li, H. Ning, O. Mehio, H. Zhao, Min-Cheol Lee, K. Kim, F. Nakamura, Y. Maeno, G. Cao, and D. Hsieh, Keldysh space control of charge dynamics in a strongly driven Mott insulator, Phys. Rev. Lett. **128**, 187402 (2022).

[36] T. Oka, Nonlinear doublon production in a Mott insulator: Landau-Dykhne method applied to an integrable model, Phys. Rev. B **86**, 075148 (2012).

[37] J.-Y. Shan, M. Ye, H. Chu, S. Lee, J.-G. Park, L. Balents, and D. Hsieh, Giant modulation of optical nonlinearity by Floquet engineering, Nature (London) **600**, 235 (2021).

[38] K. Yamada, N. Suzuki, and J. Akimitsu, Magnetic properties of $(Sr, Ba)_2Cu_3O_4Cl_2$: two-dimensional antiferromagnetic cuprates containing two types of Cu-site, Phys. B: Condens. Matter **213-214**, 191 (1995).

[39] F. C. Chou, A. Aharony, R. J. Birgeneau, O. Entin-Wohlman, M. Greven, A. B. Harris, M. A. Kastner, Y. J. Kim, D. S. Kleinberg, Y. S. Lee, and Q. Zhu, Ferromagnetic moment and spin rotation transitions in tetragonal antiferromagnetic $Sr_2Cu_3O_4Cl_2$, Phys. Rev. Lett. **78**, 535 (1997).

[40] K. L. Seyler, A. Ron, D. Van Beveren, C. R. Rotundu, Y. S. Lee, and D. Hsieh, Direct visualization and control of antiferromagnetic domains and spin reorientation in a parent cuprate, Phys. Rev. B **106**, L140403 (2022).

[41] J. W. Harter, L. Niu, A. J. Woss, and D. Hsieh, High-speed measurement of rotational anisotropy nonlinear optical harmonic generation using position-sensitive detection, Opt. Lett. **40**, 4671 (2015).

[42] M. Guarise, B. Dalla Piazza, M. Moretti Sala, G. Ghiringhelli, L. Braicovich, H. Berger, J. N. Hancock, D. van der Marel, T. Schmitt, V. N. Strocov, L. J. P. Ament, J. van den Brink, P.-H. Lin, P. Xu, H. M. Rønnow, and M. Grioni, Measurement of magnetic excitations in the two-dimensional antiferromagnetic $Sr_2CuO_2Cl_2$ insulator using resonant x-ray scattering: Evidence for extended interactions, Phys. Rev. Lett. **105**, 157006 (2010).

[43] P. Babkevich, N. E. Shaik, D. Lanon, A. Kikkawa, M. Enderle, R. A. Ewings, H. C. Walker, D. T. Adroja, P. Manuel, D. D. Khalyavin, Y. Taguchi, Y. Tokura, M. Soda, T. Masuda, and H. M. Rønnow, Magnetic excitations from the two-dimensional

interpenetrating Cu framework in $Ba_2Cu_3O_4Cl_2$, Phys. Rev. B **96**, 014410 (2017).

[44] F. Bassani and G. Pastori Parravicini, *Electronic States and Optical Transitions in Solids* (Pergamon Press, Oxford, 1975).

[45] P. A. Fleury and R. Loudon, Scattering of light by one- and two-magnon excitations, Phys. Rev. **166**, 514 (1968).

[46] Y. Tanabe, T. Moriya, and S. Sugano, Magnon-induced electric dipole transition moment, Phys. Rev. Lett. **15**, 1023 (1965).

[47] A. E. Fedianin, A. M. Kalashnikova, and J. H. Mentink, Selection rules for ultrafast laser excitation and detection of spin correlation dynamics in a cubic antiferromagnet, Phys. Rev. B **107**, 144430 (2023).

[48] D. Bossini, S. Dal Conte, G. Cerullo, O. Gomonay, R. V. Pisarev, M. Borovsak, D. Mihailovic, J. Sinova, J. H. Mentink, T. Rasing *et al.*, Laser-driven quantum magnonics and terahertz dynamics of the order parameter in antiferromagnets, Phys. Rev. B **100**, 024428 (2019).

[49] F. Formisano, T. T. Gareev, D. I. Khusyainov, A. E. Fedianin, R. M. Dubrovin, P. P. Syrnikov, D. Afanasiev, R. V. Pisarev, A. M. Kalashnikova, J. H. Mentink *et al.*, Coherent THz spin dynamics in antiferromagnets beyond the approximation of the Néel vector, APL Mater. **12**, 011105 (2024).

[50] M. Djordjevic and M. Münzenberg, Connecting the timescales in picosecond remagnetization experiments, Phys. Rev. B **75**, 012404 (2007).

[51] A. de la Torre, K. L. Seyler, M. Buchhold, Y. Baum, G. Zhang, N. J. Laurita, J. W. Harter, L. Zhao, I. Phinney, X. Chen, S. D. Wilson, G. Cao, R. D. Averitt, G. Refael, and D. Hsieh, Decoupling of static and dynamic criticality in a driven Mott insulator, Commun. Phys. **5**, 35 (2022).

[52] P. E. Dolgirev, M. H. Michael, A. Zong, N. Gedik, and E. Demler, Self-similar dynamics of order parameter fluctuations in pump-probe experiments, Phys. Rev. B **101**, 174306 (2020).

[53] T. Kawasaki, Possibility of inverse Suhl instability processes by optical pumping in antiferromagnets, J. Magn. Reson. (1969) **9**, 114 (1973).

[54] T. Odagaki, Photon pumped spin wave instability in rutile-type antiferromagnets, J. Phys. Soc. Jpn. **35**, 40 (1973).

[55] J. H. Mentink and M. Eckstein, Ultrafast quenching of the exchange interaction in a Mott insulator, Phys. Rev. Lett. **113**, 057201 (2014).

[56] N. Walldorf, D. M. Kennes, J. Paaske, and A. J. Millis, The antiferromagnetic phase of the Floquet-driven Hubbard model, Phys. Rev. B **100**, 121110(R) (2019).

[57] D. Malz, J. Knolle, and A. Nunnenkamp, Topological magnon amplification, Nat. Commun. **10**, 3937 (2019).

[58] J. B. Curtis, A. Grankin, N. R. Poniatowski, V. M. Galitski, P. Narang, and E. Demler, Cavity magnon-polaritons in cuprate parent compounds, Phys. Rev. Res. **4**, 013101 (2022).

[59] Y. Wang, C.-C. Chen, B. Moritz, and T.P. Devereaux, Light-enhanced spin fluctuations and *d*-wave superconductivity at a phase boundary, Phys. Rev. Lett. **120**, 246402 (2018).

[60] C. Schoenfeld, L. Feuerer, D. Wuhrer, W. Belzig, A. Leitenstorfer, D. Juraschek, and D. Bossini, Dynamical renormalisation of a spin hamiltonian via high-order nonlinear magnonics, arXiv:2310.19667.

[61] Y. I. Ukhanov, *Optical Properties of Semiconductors* (Nauka, Moscow, 1977).

[62] S. Toth and B. Lake, Linear spin wave theory for single-Q incommensurate magnetic structures, J. Phys.: Condens. Matter **27**, 166002 (2015).

[63] Y. J. Kim, R. J. Birgeneau, F. C. Chou, M. Greven, M. A. Kastner, Y. S. Lee, B. O. Wells, A. Aharony, O. Entin-Wohlman, I. Ya. Korenblit, A. B. Harris, R. W. Erwin, and G. Shirane, Neutron scattering study of $Sr_2Cu_3O_4Cl_2$, Phys. Rev. B **64**, 024435 (2001).

[64] R. W. Boyd, *Nonlinear Optics* (Academic Press, Cambridge, 2020).

[65] A. V. Kimel, C. D. Stanciu, P. A. Usachev, R. V. Pisarev, V. N. Gridnev, A. Kirilyuk, and T. Rasing, Optical excitation of antiferromagnetic resonance in $TmFeO_3$, Phys. Rev. B **74**, 060403(R) (2006).

[66] M. Matsubara, Y. Okimoto, T. Ogasawara, Y. Tomioka, H. Okamoto, and Y. Tokura, Ultrafast photoinduced insulator-ferromagnet transition in the perovskite manganite $Gd_{0.55}Sr_{0.45}MnO_3$, Phys. Rev. Lett. **99**, 207401 (2007).

[67] H. Yada, M. Matsubara, H. Matsuzaki, H. Yamada, A. Sawa, and H. Okamoto, Discrimination between photodoping-and heat-induced magnetization changes in $Nd_{0.52}Sr_{0.48}MnO_3$ using a heterostructure with $SrTiO_3$, Phys. Rev. B **84**, 045114 (2011).

[68] M. Ohno, T. Kawamata, M. Akoshima, and Y. Koike, Thermal conductivity due to spins in the two-dimensional spin system $Ba_2Cu_3O_4Cl_2$, J. Phys. Soc. Jpn. **88**, 064708 (2019).

[69] S. Noro, H. Suzuki, and T. Yamadaya, Magnetic properties of $Ba_{2-x}K_xCu_34Cl_2$, Solid State Commun. **76**, 711 (1990).

[70] H. Y. Hwang, P. Dai, S-W. Cheong, G. Aeppli, D. A. Tennant, and H. A. Mook, Softening and broadening of the zone boundary magnons in $Pr_{0.63}Sr_{0.37}MnO_3$, Phys. Rev. Lett. **80**, 1316 (1998).

[71] B. Normand, H. Kohno, and H. Fukuyama, Spin-phonon coupling in the single-layer extended t-*J* model, Phys. Rev. B **53**, 856 (1996).